Amplitude Distribution of Low Grazing Angle G-band Littoral Sea Clutter

1st Aleksanteri B. Vattulainen
SUPA School of Physics & Astronomy
University of St Andrews
St Andrews, Scotland
av41@st-andrews.ac.uk
https://orcid.org/0000-0003-1898-600X

2nd Samiur Rahman
SUPA School of Physics & Astronomy
University of St Andrews
St Andrews, Scotland
sr206@st-andrews.ac.uk
https://orcid.org/0000-0002-5477-4218

3rd Andrew G. Stove
School of Electronic,
Electrical & Systems Engineering
University of Birmingham
Birmingham, UK
andystove@virginmedia.com

4th Duncan A. Robertson
SUPA School of Physics & Astronomy
University of St Andrews
St Andrews, Scotland
dar@st-andrews.ac.uk
https://orcid.org/0000-0002-4042-2772

***Abstract*—G-band radar sensing of the marine environment is of interest for maritime autonomy, however at present, no phenomenological data of low grazing angle sea clutter at this frequency is available in the literature. Future sensor design is contingent on the modeling of empirical data, with polarization expected to be a key parameter. This paper presents the results of an analysis of data of radar returns from the water's surface gathered in 2022 at Coniston Water, UK. The difference in amplitude distribution and normalized radar cross section (NRCS) between HH (horizontal-horizontal) and VV (vertical-vertical) polarization is shown for two 0.5° wide grazing angle swaths centered at 2° and 4°. HH is seen to produce longer-tailed distributions than VV for both swaths, with a mean NRCS for thresholded data (i.e. for wave signal peaks) of -33.3 dB (HH) and -35.2 dB (VV) for the swath centered at 2°, and -38.6 dB (HH) and -41.6 dB (VV) for the swath centered at 4°.**

***Index Terms*—sea clutter, G-band, NRCS, low grazing angle, FMCW radar**

I. Introduction

A. Motivation

There is a growing interest in the use of radar sensors to provide situational awareness for agile autonomous marine vessels, which need short-range and high-resolution sensing. G-band (140-220 GHz) is of interest for this application due to transmission windows where most of the all-weather benefits of radar are preserved, whilst offering higher angular, range, and Doppler resolutions in a smaller instrument than a traditional maritime radar. The hardware and detection scheme design of these sensors requires knowledge of the backscatter amplitude behavior of targets and clutter. Agile vessels are generally small- to medium-sized, where sensors are a few meters above sea level with a detection range typically of the order of a hundred meters, thus specifically low grazing angle ($> 0.1°$, $\leq 10°$) sea clutter and how this varies with different measurement parameters is of interest, with polarization being the focus of this paper.

This work was supported by the UK Engineering and Physical Sciences Research Council under grant EP/S032851/1.

B. Prior Art

Extensive empirical sea clutter measurements have been made at S-, C-, and X-band (summarized in well-known textbooks such as [1], [2]) as these are the most used in marine applications. There are, however, few data above Ka-band available. Modeling of the normalized radar cross section (NRCS, also σ^0), which is used to describe the backscatter amplitude of sea clutter, has been developed from available data, where key models are detailed in [3], [4].

Published W-band results of low grazing angle backscatter amplitude include data gathered in St Andrews, Scotland in 2014 [5]. Measurements of littoral waves were conducted using a 94 GHz frequency modulated continuous wave (FMCW) scanning radar operating in either VV or HH polarization for a grazing angle of 2°-3° in sea state 3. For that data, the σ^0 was reported as -22 dB and -30 dB for wave peaks and a mean over a full wave respectively, but following a more recent calibration of that radar, the present authors discovered these results were erroneous and the values should be -12 dB and -20 dB respectively. The distribution of HH data showed that it was longer-tailed or 'spikier' than VV, meaning a greater number of excursions to high values, but that there was no difference in σ^0 between HH and VV.

A stepped frequency radar of frequency 91.5-97.5 GHz used in research by the Beijing Institute of Technology in 2019 found a σ^0 = -24.5 dB, for a sea state of 1-2 (as defined in [1]) and grazing angle of 1.2° in Qinhuangdao, China. This value was derived from peak values rather than an average over all data. Like [5], polarimetric measurements indicated that the HH amplitude distribution was longer tailed than for VV [6].

The most recently reported W-band sea clutter data were gathered by the present authors as part of the STREAM project (Sub-THz Radar sensing of the Environment for future Autonomous Marine platforms), where measurements of littoral waves in St Andrews, Scotland, were made in late 2020. That

work reported σ^0 = -48 to -12 dB (depending on scattering type) in circular polarization for a grazing angle of 1-3° in an estimated sea state of 0-1 (littoral 2) [7].

At G-band, the only published measurements of sea clutter are of high grazing angle data, collected by airborne measurements over the Santa Barbara Channel, California, in 2019 and published in 2022. These results are for an FMCW radar operating at 167 GHz in circular polarization, observing very calm conditions in a grazing angle range of 62°-90°, resulting in σ^0 ranging from a minimum of ~-45 dB up to a near-nadir mean of +14.8 dB [8].

Given that backscatter at all other frequencies has a significant grazing angle dependence [3], the results in [8] are not directly comparable to the low grazing angle case. No results are presently available in the literature for low grazing angle sea clutter above W-band, hence the need for fundamental research into the phenomenology of sea clutter backscatter at G-band to support the development of sub-THz radar sensors for marine autonomy.

This paper presents data of the radar returns from the surface of a lake. Although this is not strictly speaking 'sea clutter' the returns from the lake are assumed to be a good surrogate for the returns from the sea in the littoral zone in low sea states, and so will be referred to as 'sea clutter' in this paper. This is partly because that is the familiar term but also because, as discussed above, the ultimate aim of the work is to understand the returns from the sea.

II. Field Trial

A. Apparatus

The field trial was conducted at Coniston Water, UK, over the course of three days from 30 August 2022 - 1 September 2022. The radar and digital camera which collected coincident video were both mounted on tripods and positioned as indicated in Fig. 1, on the shore of the lake (54°20'48.1"N 3°04'33.4"W). The FMCW Doppler radar, which operates at 207 GHz, was designed and built by the Millimetre Wave Group at the University of St Andrews [9], [10]. The radar parameters are listed in Table I, and the radar is calibrated to within 2.7 dB in the range of interest.

B. Procedure

A measurement of the radar noise floor was performed on the first day of the trial by sky pointing. To gather sea clutter data, the radar and camera were first pointed at the same bearing using a compass and by reference to landmarks. The depression angle δ (of radar boresight below horizontal) of the

Fig. 1: Field trial location at Coniston Water. Radar location is just east of the Raymond Priestley Centre (RPC). The blue lines indicate the approximate range of measurement bearings.

TABLE I: Radar Parameters

Parameter	Value
Center frequency	207 GHz
Modulation	FMCW
Antenna beamwidth (two-way)	1.41°
Antenna gain	37.9 dBi
Polarization	HH or VV
Transmit power	+14.4 dBm
Noise figure	14.2 dB
Bandwidth / range resolution	2 GHz / 7.5 cm
Chirp time	51.49 µs
Chirp repetition interval	67.58 µs
Instrumented range	153.6 m

TABLE II: Swath Mean Ranges

Swath	Boresight (m)	Near Edge (m)	Far Edge (m)
2	50.9	45.2 ± 1.7	58.2 ± 2.5
4	25.5	24.0 ± 0.6	27.1 ± 0.8

instruments was set using a digital inclinometer, and the height above the water's surface was measured for both instruments. The radar acquired staring-mode data only, complemented by coincident video over the length of each capture. The wave direction with respect to radar boresight and wave heights were then estimated from the video data, as well as visually during the trial. Polarization was changed by rotation of antennas and substitution of waveguide straights with 90° twists.

C. General Conditions

The conditions during the trial were fair, being generally sunny with light cloud. Wind speeds varied from locally still to gusts measured up to 22 km/h in directions between -30° and +30° approaching the radar line of sight. Air temperatures were ~18°C. The condition of the water's surface varied from near glassy to maximum wave heights of ~10 cm, sometimes with surface roughening and breaking wave crests caused by wind, corresponding to a Douglas sea state of 1.

III. Results

For the purposes of the analysis, swaths of grazing angle were taken over 0.5° in extent around two nominal center values of 2° and 4° such that the swaths are 1.75°-2.25° and 3.75°-4.25° respectively. For brevity, these are referred to as swaths 2 and 4. The extent of 0.5° was chosen to limit the antenna gain variation and control for the σ^0 dependence on grazing angle, which for lower frequencies is typically exponential in this regime [3]. Grazing angle swaths have corresponding slant range swaths calculated as $R = h/\sin(\gamma)$, where R is the slant range, h is the radar height, and γ is the grazing angle. In the case of a run where $\delta = 2°$, boresight has a $\gamma = 2°$ and thus is at the center of swath 2. All the data were collected at a radar height of either 1.77 or 1.78 m ±0.02 m, with an uncertainty in δ of ±0.05°. Table II lists the calculated swath ranges and uncertainties, where ranges calculated for the two radar heights were averaged, and the different positive and negative uncertainties were also averaged.

The clutter data runs analyzed are assigned with shorthand labels of the form 'Polarization$_{X,Y}$', where X is the swath number and Y is the run number. All the data in the analysis were collected at a δ matching the swath center values except

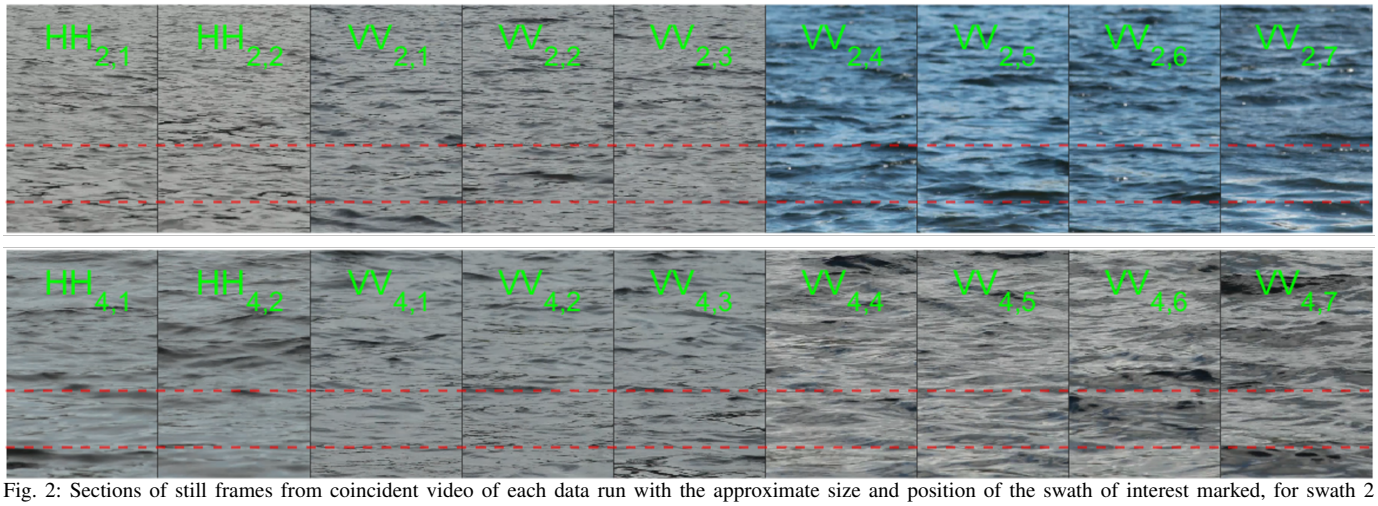

Fig. 2: Sections of still frames from coincident video of each data run with the approximate size and position of the swath of interest marked, for swath 2 (top) and swath 4 (bottom).

$HH_{2,1}$ and $HH_{2,2}$, gathered at $\delta = 2.2°$. This selection was made to minimize gain fall off in elevation pattern. A swath is then a subsection of the -3 dB contour footprint, composed of multiple range bins near boresight. As the range resolution is 7.5 cm, the extent of a range bin is much greater in azimuth than range, where the swath 2 near and far edges are 1.1 m and 1.4 m, and for swath 4 are 0.6 m and 0.7 m.

Fig. 2 shows coincident video frames for each data run, chosen to ensure consistent wave height. Some variation in wave height and surface roughness between runs relates to the varying wind speed, which was between 10-19 km/h sustained with up to 22 km/h gusts. Runs had an oncoming wave direction between -10° and +10°, centered on boresight. The wave heights were estimated from video (corroborated by observations during the trial) to vary from 5-10 cm for all the data presented; a finer resolution estimate is not possible from video so all data runs are classed as a broadly equivalent in this analysis. Run lengths varied from ~7-15 s.

The data from each run were processed into range-time-intensity (RTI) plots (flattop windowed), where truncated examples are shown in Fig. 3. The returns appear as either small patches of signal or as diagonal streaks, indicating approaching waves. The wave returns are closely linked to the surface conditions, where the very intermittent signal seen in Fig. 3 for $HH_{2,2}$ corresponds to a calmer surface relative to the others in Fig. 2. Returns are generally of a low level due to the low wave heights observed, the majority of the plot being the radar noise floor as the radar is insufficiently sensitive to detect reflections from the mostly smooth surface of the water at these grazing angles.

A. Distribution Shape

To compare the shape of the amplitude distribution in each data run, they are plotted as logarithmic probability of false alarm, $\log_{10}(\mathrm{P_{fa}})$, versus normalized threshold level, α. To generate these plots, the distributions are plotted as histograms with counts normalized to sum to unity, and then shifted for a mean value also of unity. This latter operation gives the normalized threshold on the x-axis. Y-axis values are then calculated by summing from a given α up to the top of the distribution, which gives the probability of false alarm:

$$\mathrm{P_{fa}}(\alpha) = \sum_{x=\alpha}^{\infty} y(x) \tag{1}$$

and the base 10 logarithm of this value is then plotted [4]. These plots are a representation of the complementary cumulative distribution function (CCDF), where the log scale highlights the differences in the distribution tails, important in determining the $\mathrm{P_{fa}}$ in a detection scheme. The CCDF plots for the two grazing angle swaths are shown in Fig. 4 and 5. Each run consisted of ~$2{\cdot}10^7$ or ~$5{\cdot}10^6$ samples in swath 2 and 4 respectively, thus the validity of the curves is limited below a $\mathrm{P_{fa}}$ of 10^{-6} and 10^{-5} respectively.

These distributions look the same at high $\mathrm{P_{fa}}$ as they consist mostly of noise. To avoid disrupting the shape of the noise floor it was deemed unsuitable to apply radar range calibration corrections directly to the data shown in Fig. 4 and 5. This introduces uncertainty in the shape of the distribution, which is quantified using values from Table II. The calibration curve, Fig. 6, shows the change in signal level for a point target across each swath. The change in clutter level in decibels will be ¾ of that for a point target as low grazing angle range-gate-limited clutter follows an R^{-3} law rather than R^{-4}. The variation across swath 2 will then be ±1.6 dB and ±0.6 dB for swath 4. The reduction in antenna gain off-boresight in swath 2 is 0.2 dB for $\delta = 2°$ in VV polarization, and 0.6 dB for $\delta = 2.2°$ in HH. For swath 4, the loss is 0.2 dB in both HH and VV. Accounting for both effects, the region of uncertainty around each clutter curve is then ±1.9 (HH) and ±1.7 dB (VV) for swath 2 and ±0.7 dB for all curves in swath 4.

Fig. 4 and 5 indicate that the distributions for HH polarized data are longer-tailed (spikier) than those for VV data at 207 GHz for both grazing angle swaths at these wave heights. This is consistent with results seen at lower frequencies [3] and in some data collected at W-band [5], [6]. The data appears more clustered for swath 2 than for swath 4, where for both swaths the divergence in the curves for decreasing $\mathrm{P_{fa}}$ is due to differing levels of spikiness.

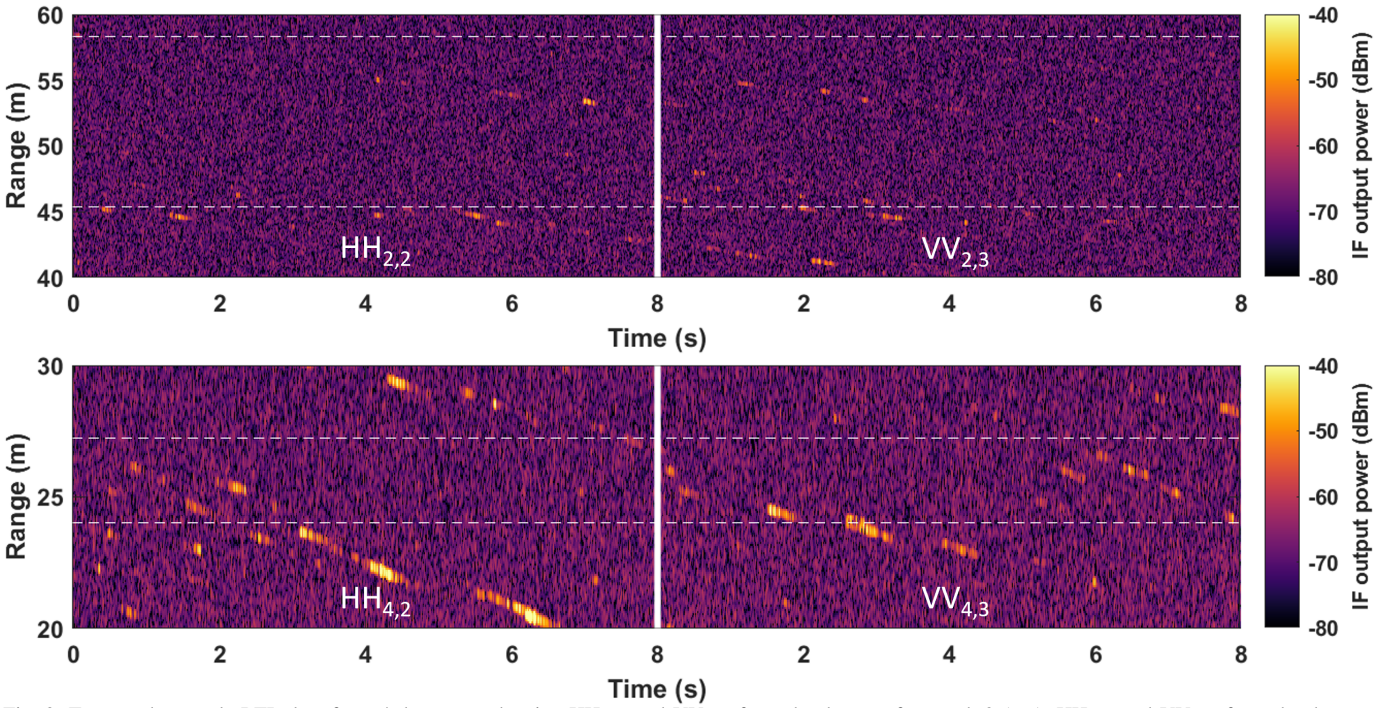

Fig. 3: Truncated example RTI plots from 4 data runs, showing $HH_{2,2}$ and $VV_{2,3}$ from the data set for swath 2 (top), $HH_{4,2}$ and $VV_{4,3}$ from the data set for swath 4 (bottom). Dashed lines indicate the range extents of the grazing angle swaths.

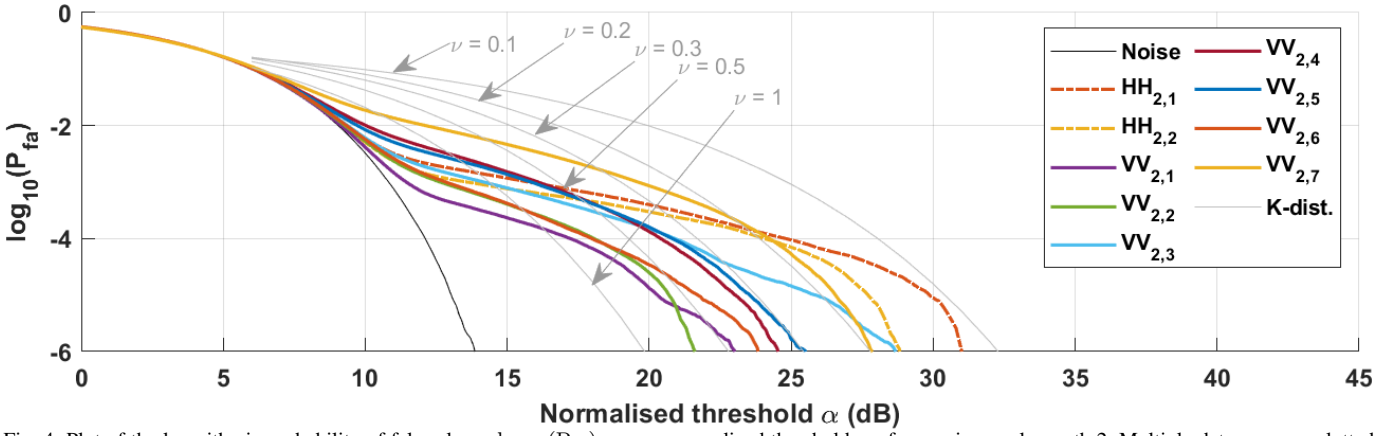

Fig. 4: Plot of the logarithmic probability of false alarm, $\log_{10}(\mathrm{P_{fa}})$, versus normalized threshold, α, for grazing angle swath 2. Multiple data runs are plotted in color and the noise floor in black, where the tails of the HH clutter data (dashed lines) are seen to be longer than those for VV (solid lines). The gray lines show curves for the K-distribution model for values of the shape parameter, ν, from 1 to 0.1 [3].

There is a large variation in the data, even for runs closely spaced in time; in Fig. 5, curves $HH_{4,1}$ and $HH_{4,2}$ were recorded within a minute of each other but show a difference of ~7 dB at a $\mathrm{P_{fa}}$=10^{-4}, and similarly the curves for $VV_{4,2}$ and $VV_{4,3}$ show a difference of ~9 dB at this level. This is possibly due to the relatively short data durations (~10 s) compared to the evolution timescale of the water's surface, i.e. the temporal averaging of the surface does not converge for these capture durations. This variability may be especially acute due to the small wave heights, often resulting in smaller and more sparse wavelets rather than full wave fronts, where the coincidence of such a wavelet with the beam was less frequent. It may also be the case that these measurements are simply very sensitive to slight variations in environmental conditions and the fluctuations in the data reflect this. There are fewer HH runs plotted, where further measurements would improve confidence in the trend as this has an uncertainty due to the relatively small number of measurements.

The noise floor statistics were confirmed to be normally distributed in each swath, so curves of the K-distribution were overlaid to estimate the shape parameters, ν, of the distribution tails. Clutter diverges from noise first into a region with a shallow gradient before a steeper region after a knee. The shallower region indicates more spikiness in the data, and that it is spikier than K-distribution curves, where these do not produce good fits and are of limited value for this data. The K+noise distribution may be a better model and this will be investigated in future, however it is unlikely to produce a better

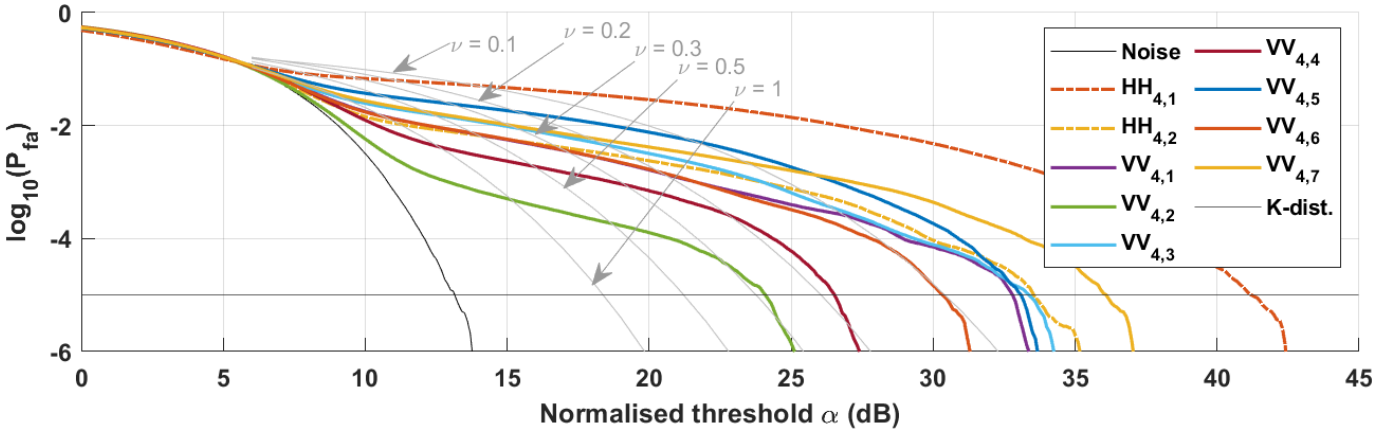

Fig. 5: Plot of the logarithmic probability of false alarm, $\log_{10}(\mathrm{P_{fa}})$, versus normalized threshold, α, for grazing angle swath 4. Multiple data runs are plotted in color and the noise floor in black, where the tails of the HH clutter data (dashed lines) are seen to be generally longer than those for VV (solid lines) but with data sets $\mathrm{VV}_{4,5}$ and $\mathrm{VV}_{4,7}$ appearing as outliers to this trend. A horizontal line has been added to indicate $\mathrm{P_{fa}}=10^{-5}$, below which the validity of the curves is limited due to the low number of samples. The gray lines show curves for the K-distribution model for values of the shape parameter, ν, from 1 to 0.1 [3].

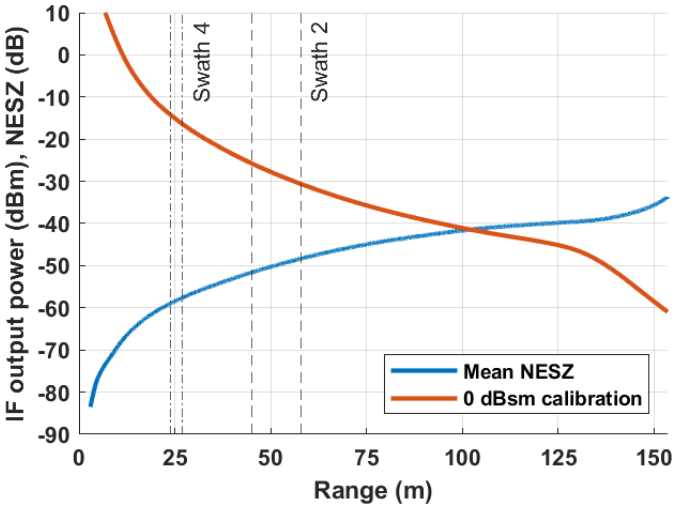

Fig. 6: Radar calibration curve matching measured points normalized for a 0 dBsm point target and the mean noise equivalent sigma zero (NESZ), with the extents of the grazing angle swaths indicated.

fit to the tails of the curves than the K-distribution given that its shape should reduce to that of the latter at high threshold values.

B. NRCS Values

NRCS values are calculated from the data by first converting return power values to radar cross section, σ:

$$\sigma(R) = \frac{x(R)}{c_1(R)c_2(R)} \tag{2}$$

where $x(R)$ are the radar data as a function of slant range R, $c_1(R)$ is a correction factor for the radar range calibration curve matched to measured data, and $c_2(R)$ corrects for the loss in gain off boresight. The calibration curve has been derived over the instrumented range and thereafter has been verified by several spot measurements with a calibrated target. The curve $c_1(R)$ is first divided by the linear σ of the target, so that the correction is applied for a target of 0 dBsm, as shown in Fig. 6. Normalizing by the area of the clutter patch, σ^0 is then calculated:

$$\sigma^0(R) = \frac{\sigma(R)}{A(R)} \tag{3}$$

where the clutter patch areas $A(R)$ are calculated using the method from Nathanson for a range-gate-limited, low grazing angle clutter patch:

$$A(R) = R\theta_{az}\Delta R \tag{4}$$

where θ_{az} is the azimuth two-way beamwidth and ΔR is the ground-range resolution [1]. Applying this calculation to the noise floor data yields the noise equivalent sigma zero (NESZ), also plotted in Fig. 6. Note that this plot does not include the correction $c_2(R)$ as this is dependent on the grazing angle swath. The plot of NESZ gives the minimum detectable σ^0 against the average noise background. Values for mean σ^0, averaged in time and range across the grazing angle swath, are presented in Tables III and IV.

The data consists of clutter plus noise, where from inspection of the RTIs in Fig. 3 it is evident that noise makes up most of the data. This is again seen in Fig. 4 and 5, where the main group of curves diverges from the noise floor at a $\mathrm{P_{fa}}$ level of ~10^{-2} and ~10^{-1} respectively, indicating a clutter to noise sample percentage of ~1% and ~10% for swaths 2 and 4

TABLE III: Swath 2 σ^0 Results

Label	Mean (dB)	s.d. (dB)	Spike (dB)	s.d. (dB)
NESZ	-49.8	5.7	-	-
$\mathrm{HH}_{2,1}$	-49.4	5.8	-33.1	3.9
$\mathrm{HH}_{2,2}$	-49.4	5.8	-33.4	4.7
HH mean	-49.4	-	-33.3	-
$\mathrm{VV}_{2,1}$	-49.7	5.7	-35.7	2.3
$\mathrm{VV}_{2,2}$	-49.6	5.7	-35.8	2.3
$\mathrm{VV}_{2,3}$	-49.6	5.7	-35.2	2.9
$\mathrm{VV}_{2,4}$	-49.4	5.8	-34.8	2.5
$\mathrm{VV}_{2,5}$	-49.5	5.7	-34.5	2.5
$\mathrm{VV}_{2,6}$	-49.6	5.7	-35.3	2.5
$\mathrm{VV}_{2,7}$	-49.1	5.9	-34.8	2.9
VV mean	-49.5	-	-35.2	-

TABLE IV: Swath 4 σ^0 Results

Label	Mean (dB)	s.d. (dB)	Spike (dB)	s.d. (dB)
NESZ	-58.1	5.6	-	-
$HH_{4,1}$	-56.3	7.8	-36.7	6.3
$HH_{4,2}$	-57.8	5.9	-40.5	4.6
HH mean	-57.1	-	-38.6	-
$VV_{4,1}$	-57.4	5.9	-41.8	3.9
$VV_{4,2}$	-57.8	5.6	-43.5	2.9
$VV_{4,3}$	-57.3	6.1	-41.4	3.9
$VV_{4,4}$	-57.0	5.8	-42.6	3.6
$VV_{4,5}$	-56.8	6.5	-39.9	4.6
$VV_{4,6}$	-57.5	5.9	-41.6	3.7
$VV_{4,7}$	-57.0	6.2	-40.7	5.0
VV mean	-57.2	-	-41.6	-

respectively. Comparing the results in Tables III and IV to Fig. 6 further confirms this as the mean σ^0 values are practically identical to the NESZ. For this reason, the typical approach employed in literature of calculating σ^0 over the whole swath is not particularly helpful in this case where almost all of the reflected power comes from small sections of the wave and the rest of the swath contains only noise. These results however imply that $\overline{\sigma^0} \ll \overline{\mathrm{NESZ}}$.

Fig. 4 and 5 can be used to determine a threshold to divide the data into a noise-like and a spike-like region, the latter of which is only clutter signal. Inspecting the noise floor curve, this threshold is set to be α=12.1 dB for a noise $\mathrm{P_{fa}} < 10^{-4}$. Above threshold, σ^0 values are calculated, as shown in Tables III and IV. The error in these values is estimated by propagating the range uncertainties in Table II. The σ calculation and area normalization together give σ^0 an R^3 dependence, for a mean uncertainty of ±0.5 dB for swath 2 and ±0.4 dB for swath 4.

These results show the mean σ^0 for the spike-like region is typically greater in HH than VV at both grazing angles, being -33.3 dB and -35.2 dB respectively in swath 2 and -38.6 dB and -41.6 dB for swath 4. Returns from waves in HH are thus greater than in VV at 207 GHz over both grazing angle swaths for the wave heights in question. The GIT [3] and APL [11] sea clutter models both show the σ^0 for these parameters at X-band to be higher in VV than HH, but predict this trend to reverse before reaching 94 GHz for the grazing angles considered. The results presented here show that this trend whereby the σ^0 in HH is higher than in VV may continue into G-band. The caveat is that these results represent only the spike-like region of the data, i.e. the tails of the distributions consisting of the highest returns, since the mean σ^0 is contaminated by noise. The true mean σ^0 values lie somewhere below the NESZ. Since we can only see the top of the distributions, this does not preclude the case where VV may have a greater true mean σ^0 with a narrower distribution (shorter tail) and HH may have a lower σ^0 with a broader distribution (longer tail).

Interestingly, the results show σ^0 is greater for the lower grazing angle swath, contrary to what is seen at lower frequencies, the difference being 5.3 dB (HH), and 6.4 dB (VV).

Curve $VV_{2,7}$ has the longest tail of VV data in swath 2, and appears as an outlier in Fig. 4, where with reference to Fig. 2 this can be attributed to a more roughened, wind rippled surface corresponding to a sustained wind speed of 19 km/h, the highest recorded for all the data analyzed. This does not however translate to a significantly higher σ^0 value than the other VV data for swath 2. In Fig. 5, curves $VV_{4,5}$ and $VV_{4,7}$ appear as outliers, with the latter having a longer tail than $HH_{4,2}$, again possibly due to surface roughening by wind (12 km/h sustained, 20 km/h gust).

IV. Conclusion

This paper has presented an analysis of the effect of linear polarization on the amplitude distribution and σ^0 of littoral sea clutter of sea state 1 for grazing angle swaths centered at 2° and 4° at 207 GHz. The data was gathered at Coniston Water, UK, in 2022. It has been shown that the HH data distribution is longer-tailed than VV for both swaths, and that K-distribution curves with a minimum shape parameter of $\nu = 0.1$ do not fit any of the data. It is shown that the true mean σ^0 in these conditions is below the NESZ of the system, implying an upper bound of -49.8 dB for grazing angle $\gamma = 2°$ and -58.1 dB for γ =4°. For clutter signals above the noise floor at $\gamma = 2°$ and $\gamma = 4°$, mean σ^0 for HH was -33.3 dB and -38.6 dB respectively, and for VV were -35.2 dB and -41.6 dB respectively. This shows the HH data has a greater σ^0 than VV, and that σ^0 was greater at $\gamma = 2°$.

In future, further measurements and analysis are planned to verify these results and investigate the effect of other parameters such as grazing angle and wave height, where such data could then be used to extend empirical sea clutter models.

Acknowledgment

The authors thank the staff at the Raymond Priestley Centre for their help over the duration of the trial.

References

[1] F. E. Nathanson, J. P. Reilly, and M. N. Cohen, *Radar design principles: Signal Processing and the Environment*, 2nd ed. SciTech Publishing, Incorporated, 1999.

[2] M. I. Skolnik, *Radar Handbook*, 3rd ed. McGraw-Hill, 2008.

[3] K. D. Ward, R. J. Tough, and S. Watts, *Sea clutter: Scattering, the K distribution and radar performance*, 2nd ed. The Institution of Engineering and Technology, 2006.

[4] L. Rosenberg and S. Watts, *Radar Sea Clutter: Modelling and Target Detection*. IET, 2021.

[5] A. G. Stove, D. A. Robertson, and D. G. Macfarlane, "Littoral sea clutter returns at 94GHz," in *2014 International Radar Conference, Radar 2014*. Institute of Electrical and Electronics Engineers Inc., 3 2014.

[6] B. X. Weidong Hu, Z. Li, Y. Liu, and Y. Zhao, "W-band Littoral Low Grazing Angle Sea Clutter Measurement," *2019 IEEE International Conference on Computational Electromagnetics, ICCEM 2019 - Proceedings*, pp. 13–15, 2019.

[7] S. Rahman, A. Vattulainen, and D. A. Robertson, "Amplitude Characteristics of Littoral Sea Clutter Data at K-band and W-band," *Proceedings of the IEEE Radar Conference*, 2022.

[8] R. J. Roy, K. B. Cooper, M. Lebsock, J. V. Siles, L. Millan, R. Dengler, R. R. Monje, S. L. Durden, F. Cannon, and A. Wilson, "First Airborne Measurements with a G-Band Differential Absorption Radar," *IEEE Transactions on Geoscience and Remote Sensing*, vol. 60, 2022.

[9] A. B. Vattulainen, S. Rahman, and D. A. Robertson, "G-band FMCW Doppler radar for sea clutter and target characterization," in *Radar Sensor Technology XXVI*, no. May. SPIE, 2022, p. 35.

[10] ——, "G-band FMCW Doppler radar for close-range environmental sensing," *In prep.*, 2023.

[11] J. P. Reilly, R. L. McDonald, G. D. Dockery, and J. Stapleton, "RF-Environment Models for the ASDAM Program," The Johns Hopkins University Applied Physics Laboratory, Tech. Rep., 1997.